THE ASTROPHYSICAL JOURNAL, 547:594–608, 2001 February 1

A SERENDIPITOUS GALAXY CLUSTER SURVEY WITH *XMM*: EXPECTED CATALOG PROPERTIES AND SCIENTIFIC APPLICATIONS

A. KATHY ROMER
Physics Department, Carnegie Mellon University, Pittsburgh, PA 15213; romer@cmu.edu
PEDRO T. P. VIANA[1]
Centro de Astrofísica da Universidade do Porto, Rua das Estrelas s/n, 4150 Porto, Portugal
AND
ANDREW R. LIDDLE[2] AND ROBERT G. MANN[3]
Astrophysics Group, Imperial College, Blackett Laboratory, Prince Consort Road, London SW7 2BZ, England, UK
Received 1999 November 28; accepted 2000 September 18

ABSTRACT

This paper describes a serendipitous galaxy cluster survey that we plan to conduct with the *XMM* X-ray satellite. We have modeled the expected properties of such a survey for three different cosmological models, using an extended Press-Schechter formalism combined with a detailed characterization of the expected capabilities of the European Photon Imaging Camera (EPIC) camera on board *XMM*. We estimate that, over the 10 yr design lifetime of *XMM*, the EPIC camera will image a total of $\simeq 800$ deg^2 in fields suitable for the serendipitous detection of clusters of galaxies. For the presently favored low-density model with a cosmological constant, our simulations predict that this survey area would yield a catalog of more than 8000 clusters, ranging from poor to very rich systems, with around 750 detections above $z = 1$. A low-density open universe yields similar numbers, though with a different redshift distribution, while a critical-density universe gives considerably fewer clusters. This dependence of catalog properties on cosmology means that the proposed survey will place strong constraints on the values of Ω_0 and Ω_Λ. The survey would also facilitate a variety of follow-up projects, including the quantification of evolution in the cluster X-ray luminosity-temperature relation, the study of high-redshift galaxies via gravitational lensing, follow-up observations of the Sunyaev-Zeldovich effect, and foreground analyses of cosmic microwave background maps.

Subject headings: cosmology: miscellaneous — galaxies: clusters: general — X-rays: galaxies

1. INTRODUCTION

Galaxy clusters are the largest gravitationally bound structures in the universe today, and they are proving to be extremely powerful cosmological probes. In the hierarchical gravitational instability picture of structure formation, massive clusters arise from the extreme tail in the distribution of density fluctuations, so their number density depends critically on the cosmological parameters that determine the initial rms width, and the evolution with redshift, of that distribution. It thus follows that the observed cluster number density can provide strong constraints on those parameters. For example, the number density of clusters at $z = 0$ currently offers the most reliable constraint (Evrard 1989; White, Efstathiou, & Frenk 1993a) on the amplitude of density perturbations on small scales, as quantified by σ_8—the rms mass fluctuation in spheres of radius 8 h^{-1} Mpc, where h is the Hubble constant, H_0, in units of 100 km^{-1} Mpc^{-1}. In addition, several authors (White et al. 1993b; Bludman 1998; Gheller, Pantano, & Moscardini 1998; Arnaud & Evrard 1999; Wu & Xue 2000) have tried to estimate the ratio of baryonic to nonbaryonic matter in the universe as a whole from the observed baryon fraction in clusters. Perhaps the most exciting prospect is the possibility (Oukbir & Blanchard 1992; Viana & Liddle 1996, 1999) of constraining the matter density Ω_0 (and perhaps $\Omega_\Lambda \equiv \Lambda/3H_0^2$, where Λ is the cosmological constant) by observing the evolution of the number density of rich clusters. A great deal of attention (Henry 1997; Bahcall & Fan 1998; Eke et al. 1998; Sadat, Blanchard, & Oukbir 1998; Borgani et al. 1999; Reichart et al. 1999b; Viana & Liddle 1999; Blanchard et al. 2000) has been paid to this issue in recent years. To date, no consensus as to the value of Ω_0 has been reached, due, in large part, to the inadequacies of the cluster catalogs currently available.

The inadequacies of current cluster catalogs motivates the creation a major new galaxy cluster catalog using ESA's *X-Ray Multi-Mirror* (*XMM*) satellite. The *XMM* satellite[4] was successfully launched on 1999 December 10. It is a multimirror instrument, comprised of three Wolter type-1 X-ray telescope modules. There is a European Photon Imaging Camera (EPIC) imaging detector in the focal plane of each of the three telescope modules. The field of view of two of the EPIC detectors is paved with seven MOS CCDs, while the third is paved with 12 pn CCDs. The MOS detectors share the focal plane of their respective telescope modules with an RGS (reflection grating spectrometer) camera. All five detectors work simultaneously, meaning that every *XMM* pointed observation will yield the type of imaging data required for serendipitous source detection. (This is in contrast to *Chandra*, which allows for either

[1] Also affiliated with the Departamento de Matemática Aplicada da Faculdade de Ciências da Universidade do Porto, Portugal.
[2] Current address: Astronomy Centre, University of Sussex, Brighton BN1 9QJ, England, UK.
[3] Current address: Institute for Astronomy, University of Edinburgh, Royal Observatory, Blackford Hill, Edinburgh EH9 3NJ, Scotland, UK.
[4] *XMM* home page: http://XMM/vilspa.esa.es/XMM.

imaging or grating observations, but not both at the same time.)

To illustrate the enhanced sensitivity of *XMM* over other X-ray satellites, we have calculated, using the FAKEIT and SHOW RATES commands in XSPEC (Version 10.00, Arnaud 1996), the *XMM*, *Chandra*, *ROSAT*, and *Einstein* count rates for an absorbed Raymond-Smith (Raymond & Smith 1977) spectrum. The Raymond-Smith model has four input parameters: electron temperature (T), metallicity (Z), redshift (z), and normalization. For this comparison, we chose $T = 1$ keV, $Z = 0.3\ Z_{\odot}$, $z = 0.1$, and set the normalization so that the model spectrum had an unabsorbed flux of 1×10^{-13} ergs s^{-1} cm^{-2} in the 0.5–2.0 keV band. Photoelectric absorption (with $n_{\rm H} = 4 \times 10^{20}$ cm^{-2}) was included via the XSPEC WABS model, which is based on cross sections presented in Morrison & McCammon (1983). The resulting count rates are as follows:

EPIC-pn (thin filter) (0.5-10 keV): 0.078 s^{-1},
Chandra-ACIS I (0.5-10 keV): 0.017 s^{-1},
ROSAT-PSPC (0.5-2.0 keV): 0.0088 s^{-1},
Einstein-IPC (0.3-3.5 keV): 0.0040 s^{-1}.

This exercise demonstrates that *XMM* is $\sim$4 times more sensitive than *Chandra*, $\sim$10 times more sensitive than *ROSAT*, and $\sim$20 times more sensitive than *Einstein*. (The response matrices used for these calculations were epn_new_rmf.fits and epn_thin_arf.fits for *XMM*,[5] w215c2r_norm.rmf and w215c2r_norm.arf for *Chandra*,[6] pspcb_gain2_256.rmf for *ROSAT*,[7] and ipc_90jun07_16ch.rsp for *Einstein*.[7])

The high sensitivity of *XMM*, combined with its wide field of view, excellent spatial resolution, and spectral coverage, make it ideal for cluster detection out to redshifts of $z = 1$ and beyond. In this paper we detail how an *XMM* cluster catalog may be constructed through serendipitous detections in archival data. By examining the many thousands of pointing observations that will be made with *XMM*, it will be possible to build up a large sample of clusters that extends to $z \gtrsim 1$. In this paper we make predictions for the numbers and types of clusters we hope to detect in the proposed *XMM* cluster survey (hereafter XCS) and discuss the impact of the resulting cluster catalog on cosmology. We estimate that the XCS will cover $\sim$800 deg^2 (§ 4.14) to an effective flux limit of $\sim 1.5 \times 10^{-14}$ ergs s^{-1} cm^{-2} and contain (if $\Omega_0 = 0.3$) more than 8000 clusters (§ 5.3).

In § 2 we compare the XCS to existing and proposed cluster surveys. In § 3 we construct a theoretical model for the cluster population, based on the extended Press-Schechter (Press & Schechter 1974) formalism of Viana & Liddle (1999). In § 4 we describe the various assumptions we have made about the instrument response and about the spatial and spectral properties of the clusters to be observed. In § 5 we describe how we estimated the sensitivity limits of the XCS and how we went on to use those limits, in combination with the results of § 3, to produce simulated cluster catalogs. Finally, in § 6 we describe some of the potential scientific applications of the XCS and discuss some of the limitations of our calculations.

[5] Available at http://xmm.vilspa.esa.es.
[6] Available at http://asc.harvard.edu.
[7] Available at http://heasarc.gsfc.nasa.gov.

Throughout this paper we assume $h = 0.5$. *XMM* count rates are quoted in the 0.5–10 keV band, and, except where stated, fluxes and luminosities are quoted in the 0.5–2.0 keV bandpass.

2. CLUSTER SURVEYS

Cluster catalogs have traditionally been constructed by identifying enhancements in the surface density of optical galaxies on the sky (e.g., Abell 1958; Abell, Corwin, & Olowin 1989). While this can be made objective and algorithmic (Dalton et al. 1992; Lumsden et al. 1992; Postman et al. 1996), the projection effects that plague this approach cannot be overcome completely (van Haarlem, Frenk, & White 1997). The small angular size of the X-ray–emitting region in a cluster core and its high contrast against the background X-ray sky make X-ray observations one of the best strategies for cluster detection.

At low redshift attention has focused on the *ROSAT* All-Sky Survey (RASS), with a number of cluster samples (Romer et al. 1994; Ebeling et al. 1996, 1988; Henry et al. 1997; Böhringer et al. 1998; De Grandi et al. 1999a, 1999b) making use of its wide areal coverage. The most ambitious of the RASS surveys is the REFLEX survey, which covers 8235 deg^2 (compared to the $\simeq$800 deg^2 covered by the XCS; see § 4.14). To date only a preliminary sample of REFLEX clusters has been published (De Grandi et al. 1999a); this sample has a flux limit of $\sim 4 \times 10^{-12}$ ergs s^{-1} cm^{-2}, includes 130 clusters, and has a maximum redshift of $z = 0.308$. A much larger sample of $\sim$800 clusters, with a flux limit of 2×10^{-12} ergs s^{-1} cm^{-2}, will be released soon (Böhringer et al. 1998). As can be shown in § 5.3, XCS will detect a similar total number of clusters at $z < 0.3$, but this will be in a smaller area and to a deeper flux limit. Further, essentially all these clusters will be accompanied with serendipitous temperature measurements (see § 5.3). By comparison, the largest complete sample of low-redshift cluster temperatures currently available contains only 50 objects (Blanchard et al. 2000).

At higher redshifts the XCS will be far superior to the RASS-based surveys, since—with the exception of the North Ecliptic Pole (NEP) survey—the RASS-based surveys do not have the sensitivity to detect clusters beyond $z \gtrsim 0.3$. The NEP survey has higher sensitivity ($\sim 1 \times 10^{-13}$ ergs s^{-1} cm^{-2}; Gioia 1998) than REFLEX due to the scanning strategy of *ROSAT* and has yielded detections of clusters as distant as $z = 0.81$ (Henry et al. 1997). Despite this enhanced sensitivity, the NEP survey cannot compete with the XCS, since the XCS will cover roughly 10 times the area (800 deg^2 compared to 84.7 deg^2) to roughly 10 times the depth.

Data deeper than the RASS therefore are required to detect high-redshift clusters in significant numbers, and several surveys have sought them through serendipitous detections in the fields surrounding *Einstein* and *ROSAT* targets. The *Einstein* Medium-Sensitivity Survey (EMSS) has the largest areal coverage of any of these (734 deg^2 above a 0.3–3.5 keV flux limit of 3.57×10^{-12} ergs s^{-1} cm^{-2}, falling to 40 deg^2 above 1.33×10^{-13} ergs s^{-1} cm^{-2}) yielding a total of 104 clusters (Gioia et al. 1990; Henry et al. 1992). The measurement of temperatures for several of these clusters with redshifts above 0.3 (e.g., Henry 1997) has led to the wide use (e.g., Henry 1997; Bahcall & Fan 1998; Eke et al. 1998; Donahue & Voit 1999; Reichart et al. 1999b; Viana & Liddle 1999; Blanchard et al. 2000) of the

EMSS in the estimation of Ω_0, the lack of consensus in the resulting constraints indicating, at least in part, the difficulty of using the EMSS data for such a task.

More recently a number of surveys (Castander et al. 1995; Collins et al. 1997; Jones et al. 1998; Rosati et al. 1998; Vikhlinin et al. 1998a; Romer et al. 2000) have been created from serendipitous detections in pointed *ROSAT*-PSPC observations. These surveys go much deeper than the EMSS but over smaller areas; the largest single survey is the Bright SHARC survey of Romer et al. (2000), which covers 179 deg^2 to a flux limit of $\simeq 2 \times 10^{-13}$ ergs s^{-1} cm^{-2}. The deepest survey, the *ROSAT* Deep Cluster Survey, of Rosati et al. (1998) reaches a flux limit of $\sim 4 \times 10^{-14}$ ergs s^{-1} cm^{-2} over an area of ~ 50 deg^2.

As we detail below, the XCS will detect much larger numbers of high-redshift clusters than the existing *Einstein* and *ROSAT* serendipitous surveys. The XCS will benefit not only from the increased sensitivity of *XMM* over *Einstein* and *ROSAT* (see § 1) but also from *XMM*'s excellent spatial and spectral resolution. These advantages would also be shared by an *XMM* slew survey of the sort proposed by Jones & Lumb (1998).[8] However, we note that the relatively shallow depth of an *XMM* slew survey ($\sim 2 \times 10^{-13}$ ergs s^{-1} cm^{-2}) means that it would detect few high-redshift clusters and thus have little power to discriminate between cosmological models.

3. A MODEL FOR THE CLUSTER POPULATION

Our theoretical model for the cluster population uses the extended Press-Schechter (Press & Schechter 1974) formalism of Viana & Liddle (1999). The validity of this general approach has been demonstrated by comparison with N-body simulations (Eke, Cole, & Frenk 1996; Colberg et al. 1998; Tormen 1998). We refer the reader to Viana & Liddle (1999) for a more detailed description of the method.

We consider herein the following three cosmological models:

1. The currently favored spatially flat, low-density cosmology with $\Omega_0 = 0.3$ and $\Omega_\Lambda = 0.7$.
2. The Einstein–de Sitter critical density cosmology with $\Omega_0 = 1$ (and $\Omega_\Lambda = 0$).
3. An open cosmology with $\Omega_0 = 0.3$ ($\Omega_\Lambda = 0$).

We note that throughout this paper we calculate luminosity and angular diameter distances as follows: For the two $\Omega_\Lambda = 0$ models, we use the standard exact form due to Mattig (1958). For the model with nonzero Ω_Λ, we use the approximate form derived by Pen (1999). This form is perfectly adequate for our purposes, since it has an error of $\lesssim 1\%$ for flat cosmologies.

We assume that structure formation proceeds through gravitational instability from a Gaussian distribution of primordial density perturbations with a scale-invariant power spectrum. The extended Press-Schechter formalism enables us to compute the number density of clusters as a function of redshift. The version we use (Viana & Liddle 1999) includes a tracking of the merger histories of clusters in order to account properly for their time of formation when relating their mass to their temperature. The mass to temperature conversion is normalized so as to reproduce the results from the hydrodynamical simulations of White et al. (1993b) and Bryan & Norman (1998), with the extension to open or flat cosmologies with an arbitrary value for Ω_0 performed using the expressions given in Viana & Liddle (1996). In the following discussion we have only included systems with $T > 2$ keV because the Press-Schechter formalism becomes unreliable at low temperatures.

There is a weak dependence of Press-Schechter results on the current shape of the linear power spectrum of density fluctuations, so, for definiteness, we have used a cold dark matter power spectrum with shape parameter Γ (Efstathiou, Bond, & White 1992) equal to 0.23, as suggested by some analyses of galaxy clustering (Peacock & Dodds 1994; Viana & Liddle 1996; but see Mann, Peacock, & Heavens 1998). The normalization of the power spectrum is that of Viana & Liddle (1999), ensuring that the present-day abundance of high-temperature clusters is recovered. Similar cluster-based normalizations were also obtained by Eke et al. (1996); Pen (1998); Borgani et al. (1999); Blanchard et al. (2000); and Henry (2000). Further, these models give a good fit to the *COBE* 4 yr data (e.g., Tegmark 1996).

In Figure 1 we plot the cumulative number N of clusters with temperatures greater than 2, 4, and 6 keV in the whole sky as function of flux cut f for the three cosmologies. To derive the $N(f)$ functions from the Press-Schechter results we have to assume a conversion from cluster temperature to luminosity. For this we use the empirical cluster luminosity-temperature relation derived by Allen & Fabian (1998, hereafter AF98):

$$T = 1.66 L_X^{0.429} , \quad (1)$$

where the temperature T is in keV and the bolometric luminosity L_X in is units of 10^{44} ergs s^{-1}. Observations to date present no evidence for significant evolution of the L_X-T relation out to $z \sim 0.4$ (Mushotzky & Scharf 1997; AF98; Reichart, Castander, & Nichol 1999a), but nothing is known beyond that. For the purposes of our calculations, we assume that equation (1) holds at all redshifts but stress (as discussed further in § 6) that one of the principal scientific results of the XCS will be a greatly improved understanding of the L_X-T relation and its evolution with redshift.

In Press-Schechter theory, the *relative* abundance of galaxy clusters of a given mass at two given redshifts depends only on the growth rate of perturbations, which in turn depends only on Ω_0 and Ω_Λ. Figure 1 shows that $N(f)$ varies among the three cosmologies more dramatically as temperature increases (note the different scales in the three panels). Moreover, below $T \simeq 4$ keV, it is possible that the mass-temperature relation has been significantly influenced by heat injection into the intergalactic medium. For these reasons, we will largely focus our discussion on clusters with X-ray temperatures in excess of 4 keV (or luminosities $\gtrsim 2.6 \times 10^{44}$ ergs s^{-1}, based on the AF98 L_X-T relation), although we note that, in practice, the optimum (i.e., the one that minimizes the errors on cosmological-parameter estimates) temperature limit for the XCS will probably not be exactly 4 keV.

From Figure 1 it is clear that distinguishing between high and low values of Ω_0 is relatively straightforward but that discriminating between open and flat models with the same value of $\Omega_0 = 0.3$ is much harder. To do so one needs to have access to clusters at sufficiently high redshift, as illustrated by Figure 2, which shows the cumulative flux dis-

[8] The Jones & Lumb (1998) article can be found in the proceedings of the First XMM Workshop, available at http://astro.estec.esa.nl/XMM/news/ws1/ws1_papers.html.

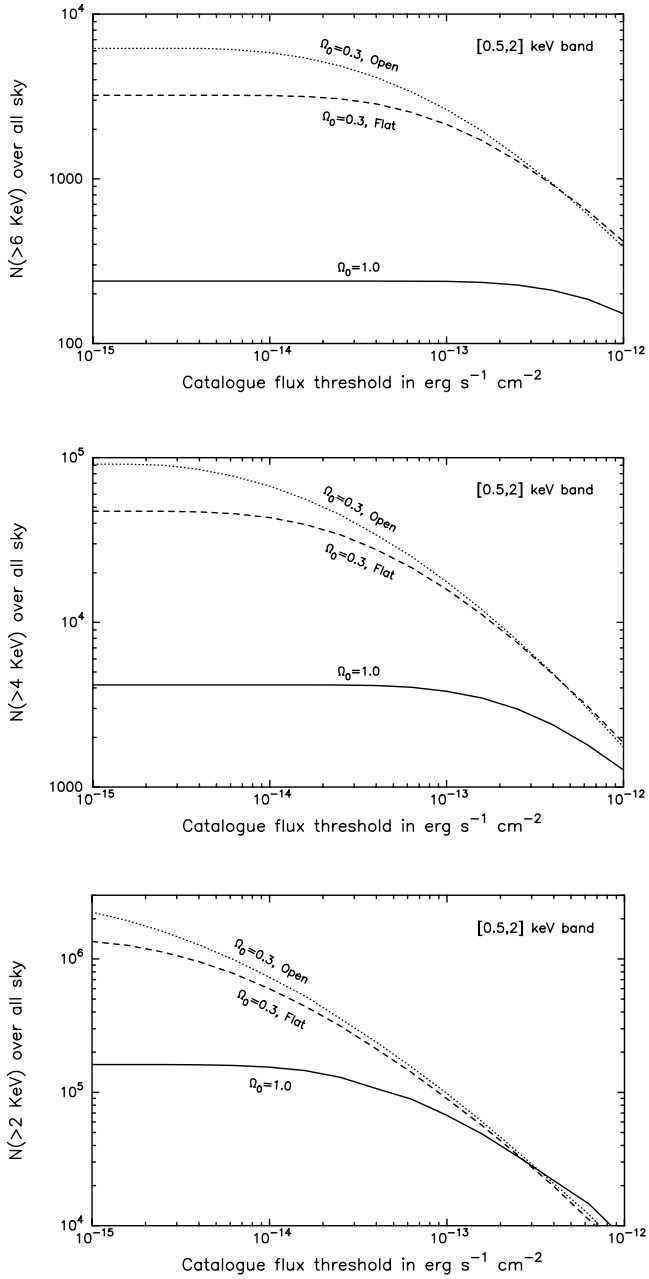

FIG. 1.—Expected number of galaxy clusters across the whole sky with X-ray temperatures in excess of 6 keV (*upper panel*), 4 keV (*middle panel*), and 2 keV (*lower panel*), as a function of the catalog flux threshold in the 0.5–2.0 keV band. The $\Omega_0 = 1$ case is the solid line, while for $\Omega_0 = 0.3$ the flat case is shown as dashed line and the open case as a dotted line.

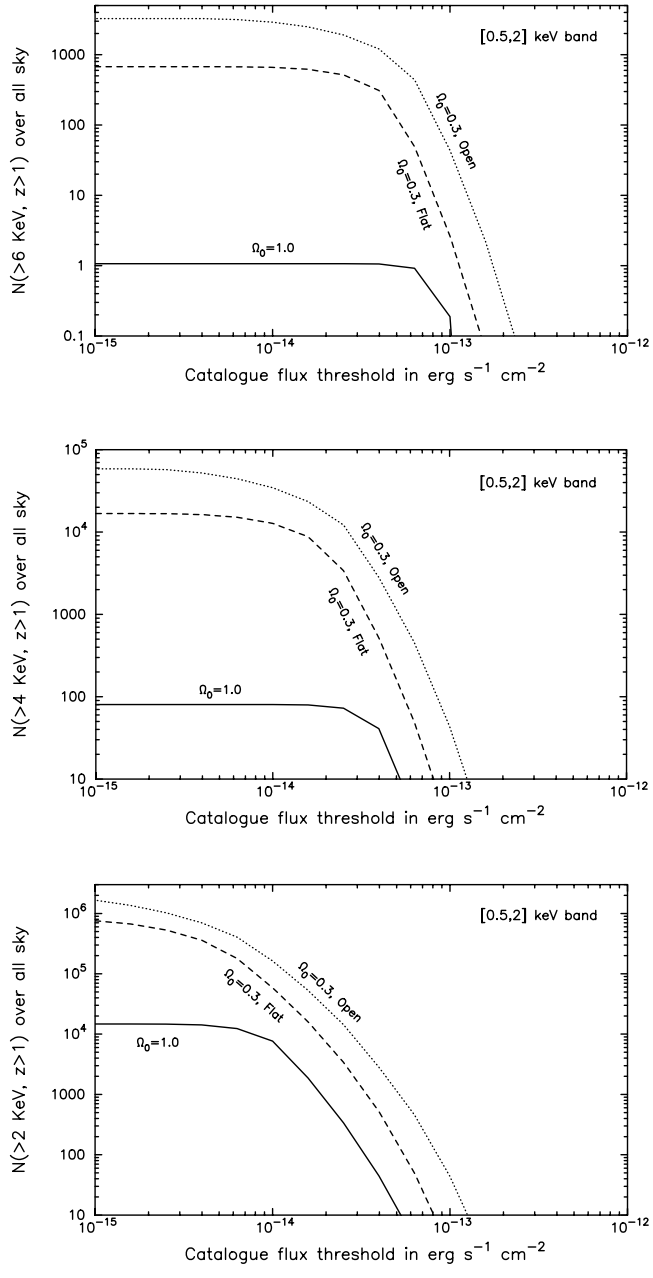

FIG. 2.—Same as Fig. 1, but showing only clusters with $z > 1$

tribution of clusters at $z > 1$; the predicted numbers of $T > 6$ keV clusters at $z > 1$ in the two $\Omega_0 = 0.3$ models differ by as much as a factor of 4 at faint flux limits, compared to less than a factor of 2 for $z > 0$. In Figure 3 we plot the analogous curves for clusters at $z < 0.3$ to demonstrate that cluster catalogs limited to low redshift (such as those produced by the various RASS-based surveys or that to be produced by the Sloan Digital Sky Survey of Gunn et al. 1998) are very poor at constraining cosmological parameters; it is necessary to reach $z \gtrsim 0.5$ to get a sufficiently long lever arm in cosmological time for the sensitivity of the growth rate of density perturbations to cosmology to become apparent.

The curves plotted in Figure 3 are flat for fluxes fainter than $\sim 10^{-13}$ ergs s^{-1} cm^{-2}, indicating that all $z < 0.3$ clusters with temperatures above $T = 2$ keV can be detected above that flux limit. This is no surprise, of course; by assumption (through eq. [1]) clusters above a certain temperature also exceed a certain luminosity, so there clearly must be a flux level at which they are all visible if a redshift limit is imposed. What is more interesting is that this asymptoting behavior is also seen in the curves in Figure 1, for which there is no redshift limit. The leveling off of the curves in Figure 1 results from the fact that clusters do not exist at arbitrarily high redshifts in a hierarchical universe; it takes a certain amount of time to accumulate the matter making up a cluster of a given mass (and, hence, temperature and luminosity). So, if one can reach a sufficiently faint flux limit, one can look along one's past light cone beyond the epoch when the first cluster of a particular

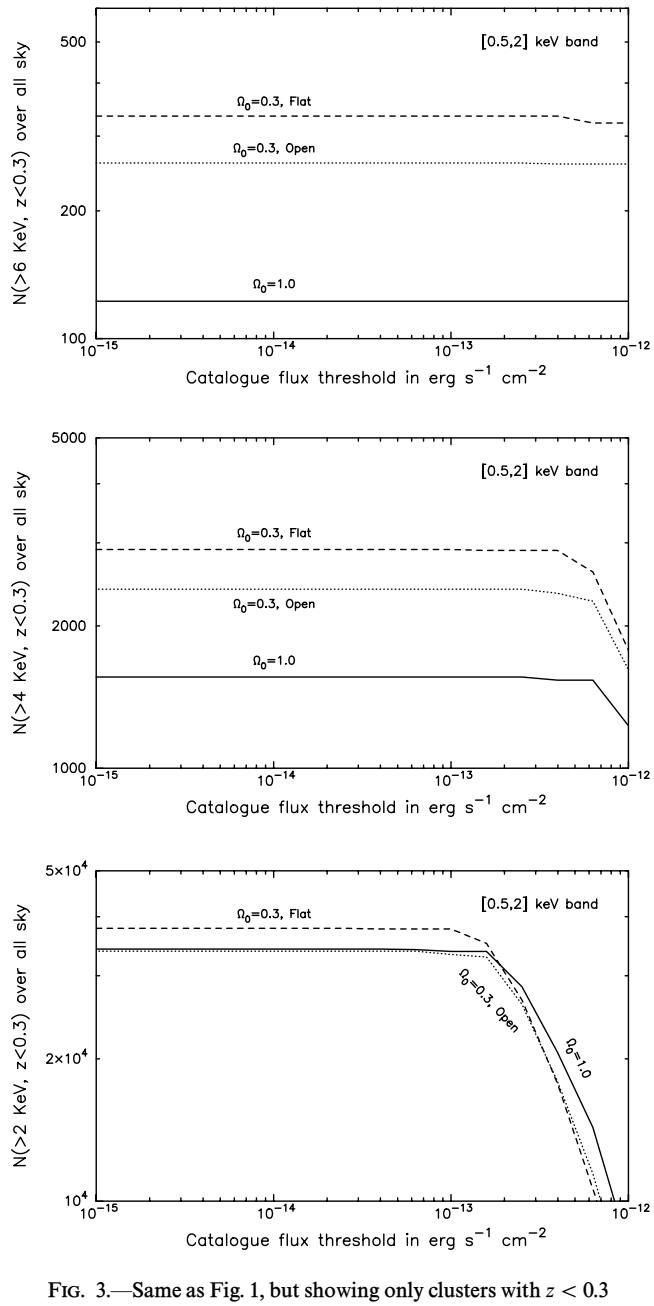

FIG. 3.—Same as Fig. 1, but showing only clusters with $z < 0.3$

mass was formed. For the high temperature ($T > 4$ keV) clusters important for cosmological-parameter estimation, this asymptote is being reached at a depth ($\sim 10^{-14}$ ergs s^{-1} cm^{-2}) that is comparable to that to be reached by the XCS (§ 5.3). This implies that there would be no point in ever performing a deeper survey than the XCS if the sole purpose of that survey was to detect $T > 4$ keV clusters; only a survey with a wider sky coverage would yield more detections (and hence tighter constraints on Ω_0 and Ω_Λ). Although we note that, by going deeper, one can obtain useful information about individual clusters such as their spatial morphology and their temperature profile.

4. ASSUMPTIONS AND SIMPLIFICATIONS MADE WHEN SIMULATING THE SENSITIVITY LIMITS OF THE XCS

In § 3 we predicted the number of clusters on the sky, N, as a function of X-ray flux, f. If clusters were the only sources in the X-ray sky, then $N(f)$ would describe the cluster catalog resulting from the idealized situation of an all-sky survey performed by an instrument with no internal background, a vanishingly narrow point-spread function (so that confusion noise is zero) and a uniform flux limit. In reality, the XCS will have a nonuniform flux limit, only will cover a fraction of the sky, and will have to detect clusters against a significant X-ray background. Moreover, since the X-ray sky is dominated by point sources (e.g., AGN), a crucial step in its construction will be the differentiation of pointlike from extended sources.

So, in order to predict how many, and what type of, clusters will be included in the XCS catalog, we need to make various assumptions about the sensitivity and spectral response of the instrument, about the surface brightness profiles and spectral properties of the clusters we expect to observe, and about the properties of the X-ray background. We detail these and other assumptions below.

4.1. *EPIC-pn Only*

We have simplified our calculations by concentrating only on the EPIC-pn camera. This is because the EPIC-MOS cameras receive only 50% of the flux from their respective telescope modules (the other 50% in each goes to an RGS) and because the MOS CCDs are intrinsically less sensitive than the pn CCDs. An additional advantage is that the simulation of the catalog-selection function will also be simplified if data from only one camera are used. However, once the clusters have been detected, the EPIC-MOS data can be used to help parameterize the cluster morphology and spectrum. By prudent use of the EPIC-MOS data, the percentage of clusters with accompanying temperatures should increase over that suggested by Table 4.

4.2. *Minimum Detection Threshold of* 8 σ

We adopt a minimum detection threshold of 8 σ. This is because the XCS will have to rely on source extent to differentiate clusters from pointlike X-ray sources, such as stars and AGN, and it has been shown (e.g., G. Wirth 1999, private communication) that extent measures can only be derived with confidence for sources detected at $\gtrsim 8$ σ. The Bright SHARC survey (Romer et al. 2000) also used a minimum detection threshold of 8 σ for this reason.

4.3. *Detection Significance Computed Using Inner 50% of Flux*

When calculating the detection significance, we consider only the inner 50% of the total cluster flux. (We define the radius of the region enclosing this flux as r_{50}.) This is because automated source-detection algorithms tend to underestimate the count rates of extended sources. For example, the wavelet-transform method adopted by the Bright SHARC survey to analyze *ROSAT* data underestimates the count rate of $z > 0.15$ clusters by a factor of 2.1 (Romer et al. 2000). This is a conservative assumption; we would hope that more efficient cluster-selection algorithms will be developed to make full use of the higher quality *XMM* data.

4.4. *Clusters Follow Spherically Symmetric Isothermal* $\beta = \frac{2}{3}$ *Model*

To estimate r_{50} values, we assume that all clusters can be modeled as spherically symmetric systems that follow an

isothermal β-profile:

$$I = \frac{I_0}{[1 + (r/r_c)^2]^{3\beta - 1/2}}, \quad (2)$$

where I is the surface brightness at radius r, r_c is the core radius, and -3β is the asymptotic radial falloff of the intracluster medium (ICM) density distribution. We adopt $\beta = \frac{2}{3}$ throughout, since this is a typical value for rich clusters (Jones & Forman 1992; Mohr, Mathiesen, & Evrard 1999), although we note that its value for any given cluster can vary in the range $0.4 \lesssim \beta \lesssim 0.9$. For a cluster described by equation (2), $\beta = \frac{2}{3}$ gives $r_{50} = \sqrt{3} r_c$. We adopt this model for the cluster surface brightness, since it has been shown (e.g., Mohr et al. 1999) to describe the *azimuthally averaged* cluster emission in the ROSAT bandpass (0.5–2.0 keV) very well. However, as we discuss in § 6.2.3, the use of such a simplistic model is one of the major limitations of our calculations.

4.5. *Nonevolving Core Radius-Luminosity Relation*

We further assume that the core radius follows the relation

$$r_c = \frac{250}{h_{50}} \left(\frac{L_{44}}{5} \right)^{0.2} \text{kpc}, \quad (3)$$

where L_{44} is the rest-frame luminosity in the 0.5–2.0 keV band in units of 10^{44} ergs s^{-1}. This relation was proposed by Jones et al. (1998) and has been shown to agree with measured values of r_c for clusters with luminosities in the range 10^{43}–10^{45} ergs s^{-1}. We assume that the core radius does not evolve (as shown by Vikhlinin et al. 1998b). A better understanding of the luminosity-core radius relation (in particular, whether it evolves with redshift) should result from forthcoming observations of known clusters with *Chandra* and *XMM*.

4.6. *Cluster Count Rates*

To determine how the *XMM* count rate varies with cluster parameters, we used the FAKEIT and SHOW RATES commands in XSPEC and assumed that the cluster X-ray emission can be described by absorbed Raymond-Smith spectra. We calculated unabsorbed fluxes and on-axis *XMM* count rates for spectra with 12 different temperatures (1 keV $< T <$ 12 keV in 1 keV increments) and 40 different redshifts ($0.05 < z < 2.0$ in $\Delta z = 0.05$ increments): 480 spectra in all. Throughout we kept the metallicity fixed at $Z = 0.3\ Z_\odot$ (see § 4.10), the normalization fixed at 1, and the Galactic H I column density fixed at $n_{\rm H} = 4 \times 10^{20}$ cm^{-2} (see § 4.11). The IGNORE command was used to limit the count rate calculation to the 0.5–10 keV band. (The full energy range over which EPIC-pn is sensitive is 0.1–11 keV.)

These 480 calculations provided us with the count rate to flux-conversion factors that were used to define the survey sensitivity limits in § 5. To illustrate how these conversion factors vary with T and z, we provide some examples: A Raymond-Smith spectrum with an unabsorbed flux of 1×10^{-13} ergs s^{-1} cm^{-2} will yield 0.078 EPIC-pn counts s^{-1} (0.5–10 keV) when $T = 1$ keV and $z = 0.1$. A spectrum with the same flux will yield 0.071 counts s^{-1} when $T = 1$ keV and $z = 1$, 0.100 counts s^{-1} when $T = 10$ keV and $z = 0.1$, and 0.093 counts s^{-1} when $T = 10$ keV and $z = 1$.

We note that the AF98 $L_{\rm X}$-T relation used in § 3 was constructed using a slightly different plasma model to that used here: MEKAL (Kaastra & Mewe 1993) in XSPEC rather than RAYMOND. However, this does not present a problem for this study since we limit our discussion to $T > 2$ keV clusters (the predictions of MEKAL and RAYMOND are very similar above $T \gtrsim 1$ keV).

4.7. *Cosmic-Background Count Rate*

We calculated the cosmic background using a model that includes two thermal Galactic components (modeled with absorbed Raymond-Smith spectra) and a power-law extragalactic component. The first thermal component had a temperature of 0.0258 keV, a metallicity of $Z_\odot$, a redshift of $z = 0$, a normalization of 2.5×10^{-6}, and a hydrogen column density of $n_{\rm H} = 1 \times 10^{17}$ cm^{-2} (Labov & Bowyer 1991). The second thermal component had a temperature of 0.0947 keV, a metallicity of $Z_\odot$, a redshift of $z = 0$, a normalization of 3.0×10^{-6}, and a hydrogen column density of $n_{\rm H} = 6 \times 10^{19}$ cm^{-2} (Rocchia et al. 1984). The power-law component had an index of $\alpha = 1.4$, a normalization of 9.32×10^{-7} (Chen, Fabian, & Gendreau 1997), and a hydrogen column density of $n_{\rm H} = 4 \times 10^{20}$ cm^{-2}. The adopted cosmic-background model yields a count rate of 2.6×10^{-3} s^{-1} arcmin^{-2} in the 0.5–10 keV band. We note that when calculating the signal-to-noise ratio of cluster detections we adjust the cosmic-background count rate by the appropriate vignetting factor (see § 4.9). The true external background (made up of solar, Galactic, and extragalactic components) is known to vary considerably across the sky, but most of this variation is confined to low energies (<1 keV, Snowden et al. 1997), and so this should not have a significant effect on the average signal-to-noise ratio values for cluster detections we calculate in the 0.5–10 keV band.

4.8. *Particle-Background Count Rate*

We calculated the particle background using the expected internal background rates quoted in the *XMM Users' Handbook*[9]: 3.0×10^{-4} counts cm^{-2} s^{-1} keV^{-1} for the EPIC-pn detector. The spectrum of the internal background is expected to be flat, so the integrated count rate in the 0.5–10 keV band is $9.5 \times 3.0 \times 10^{-4}$ counts cm^{-2} s^{-1}. We then converted from cm^{-2} to arcmin^{-2} to obtain a rate of 1.4×10^{-4} counts s^{-1} arcmin^{-2} (4.″1 corresponds to 150 μm at the detector).

4.9. *Vignetting Correction*

The count rate to flux-conversion factors calculated using XSPEC (§ 4.6) refer to the on-axis response of the EPIC-pn. In order to account for how these conversion factors vary with off-axis angle, we had to calculate vignetting corrections. We did this as follows: using the QUICKSIM[10] package written by S. Snowden, we created fake EPIC-pn images of a point source, with a Raymond-Smith spectrum, in the absence of particle and cosmic backgrounds. By placing the source at various places in the field of view, we were able to measure how the count rate varied as a function of off-axis angle. The vignetting factor changes smoothly across the field of view, so we decided to break up the field of view into five 3′ wide annuli ($\bar{\theta} = 1.'5, 4.'5, 7.'5, 10.'5,$

[9] Available at http://xmm.vilspa.esa.es/user/uhb_top.html.
[10] Available at http://legacy.gsfc.nasa.gov.

and 13′.5, respectively). For each annulus, we calculated the mean vignetting factor for a point source with a $T = 4$ keV spectrum; this was found to be 0.987, 0.892, 0.734, 0.578, and 0.520, respectively. We used a single temperature for this calculation because we found the vignetting factor to be essentially independent of temperature; the on-axis sensitivity is 2.09 times that of the sensitivity at $\theta = 12'$ for a $T = 1$ keV spectrum, compared to 2.14 for a $T = 8$ keV spectrum. We also made a megasecond QUICKSIM simulation of the cosmic background, in the absence of sources and a particle background, to confirm that these average vignetting factors also apply to the cosmic background.

4.10. *Constant ICM Metallicity: $Z = 0.3\ Z_\odot$*

The X-ray emission from an astrophysical plasma is a function of its metallicity. For example, we calculate that for a Raymond-Smith spectrum with an unabsorbed flux of 1×10^{-13} ergs s^{-1} cm^{-2}, the count rate varies from 0.077 to 0.078 to 0.079 s^{-1} for $Z = 0.1$, 0.3, and $Z_\odot$, respectively ($T = 1$ keV, $z = 0.1$, $n_{\rm H} = 4 \times 10^{20}$ cm^{-2}). Because of this weak dependence of count rate on metallicity, we adopt a constant value of $Z = 0.3\ Z_\odot$, since this is typical of rich clusters; Fukazawa et al. (1998) found that the ensemble-averaged iron abundance was 0.3 ± 0.02 based on *ASCA* observations of 40 nearby clusters of galaxies. Further, we assume that metallicity does not evolve; up to $z \sim 1$ there is observational support for this from Tsuru et al. (1997) and Schindler (1999) and theoretical support from calculations by Martinelli, Matteucci, & Colafrancesco (2000).

4.11. *Constant* H I *Column Density: $n_{\rm H} = 4 \times 10^{20}$ cm^{-2}*

Neutral hydrogen gas along the line of sight toward a cluster, particularly within our own Galaxy, absorbs a large fraction of the emitted X-rays at low ($\lesssim$0.5 keV) energies. Since we do not know what the actual distribution of hydrogen column densities will be in the XCS, we have adopted a single value, $n_{\rm H} = 4 \times 10^{20}$ cm^{-2}, which is typical for high Galactic latitudes.

The effect of column density on count rates is not large. For Raymond-Smith spectra with unabsorbed fluxes of 1×10^{-13} ergs s^{-1} cm^{-2}, the count rate varies from 0.086 to 0.078 to 0.064 s^{-1} for $n_{\rm H}$ equal to 1×10^{20}, 4×10^{20}, and 10×10^{20} cm^{-2}, respectively ($Z = 0.3\ Z_\odot$, $T = 1$ keV, $z = 0.1$). Our adoption of 4×10^{20} cm^{-2} is on the conservative side; many of the regions explored by *XMM* will have lower $n_{\rm H}$ values. For example, of the 37 clusters in the Bright SHARC survey (Romer et al. 2000), all but nine were detected in regions with $n_{\rm H} < 4 \times 10^{20}$ cm^{-2}. This means that the number of clusters eventually detected by the XCS could well be higher than suggested by Table 4.

4.12. *EPIC Thin Filter Used for All Observations*

The EPIC cameras are sensitive not only to X-rays but also to optical photons. Optical blocking filters (thin, medium, or thick) are used to minimize the number of photons entering the detector. For our calculations, we use the response functions corresponding to the thin filter only.

The choice of optical filter has an even smaller effect on count rates than column density. For a Raymond-Smith spectrum with an unabsorbed flux of 1×10^{-13} ergs s^{-1} cm^{-2}, the count rates vary from 0.078 to 0.076 to 0.06 s^{-1} when the thin, medium, and thick filters are respectively in place ($Z = 0.3\ Z_\odot$, $T = 1$ keV, $z = 0.1$, $n_{\rm H} = 4 \times 10^{20}$ cm^{-2}). To calculate the count rate through the thin, medium, and thick filters we used the files epn_thin_arf.fits, pn_med_arf.fits, and epn_thick_arf.fits,[11] respectively. It is unlikely that any *XMM* pointings that require the thick filter (i.e., those with bright stars in their field of view) will be suitable for serendipitous cluster detection, and so we can safely discount the effects of filter choice on the cluster numbers presented in Table 4.

4.13. *Bolometric and K-Corrections*

We calculated K-corrections and bolometric corrections using XSPEC. The K-correction was defined as the ratio of the unabsorbed flux in the observed energy band to the unabsorbed flux in the redshifted energy band:

$$K_{\rm lo-hi} = \frac{\int_{\rm lo}^{\rm hi} f_\nu\, d\nu}{\int_{\rm lo(1+z)}^{\rm hi(1+z)} f_\nu\, d\nu}\,, \tag{4}$$

where lo and hi are the limits of the observed energy band, e.g., 0.5 and 10.0 keV. When calculating K-corrections, the redshift of each Raymond-Smith spectrum was set to $z = 0$. Quadratic fits to the K-corrections, as a function of $(1 + z)$, were derived for each of the input temperatures (1–12 keV):

$$K_{\rm lo-hi} = c + b(1 + z) + a(1 + z)^2\,, \tag{5}$$

where a, b, and c are the coefficients of the fits; see Table 1.

The bolometric correction was defined as the ratio of the unabsorbed flux in a pseudobolometric band of 0.01–50 keV to the unabsorbed flux in the observed energy band, i.e.,

$$B_{\rm lo-hi} = \frac{\int_{0.01}^{50} f_\nu\, d\nu}{\int_{\rm lo}^{\rm hi} f_\nu\, d\nu}\,. \tag{6}$$

Setting the redshift of the Raymond-Smith spectrum to $z = 0$, B values were calculated for each of the 12 input temperatures. The bolometric corrections are listed in Table 2 for the 0.5–2.0 and 0.5–10 keV energy bands.

To illustrate how the bolometric and K-corrections were applied, we provide an example. Consider a cluster with temperature $T = 4$ keV, a redshift of $z = 1$, and an unabsorbed flux in the 0.5–2.0 keV (observed) band of 1×10^{-13} ergs s^{-1} cm^{-2}. The K-corrected flux in the 0.5–2.0 keV (rest-frame) band is 0.836×10^{-13} ergs s^{-1} cm^{-2} (from eq. [5] and Table 1). The bolometric flux for this cluster is then 3.04 times this, from Table 2.

4.14. *Exposure-Time Distribution and Area of the Survey*

In § 5.3 we combine our sensitivity-limit calculations (§§ 5.2 and 5.1) with our model cluster population (§ 3) in order to predict the properties of the XCS. To do so requires us to assume both an areal coverage and an exposure-time distribution for the survey. We do not know what the exposure-time distribution will be for the thousands of pointings that will eventually comprise the *XMM* archive. So, for the purposes of this paper, we assume that the exposure times will be distributed in the same way as they are for 760 pointings in the *XMM* guaranteed time observations (GTO; Table 3). The 760 GTO pointings have exposure times that range from 5 to 95 ks, with an average of 22.3 ks. For comparison, we also list in Table 3 the distribution of the exposure times in the *XMM* A01 program.

For the areal coverage, we use a total value of 800 deg^2 (as justified below). However, we note that our treatment of

[11] All available at http://xmm.vilspa.esa.es.

TABLE 1

COEFFICIENTS OF THE QUADRATIC FITS TO *K*-CORRECTIONS FOR RAYMOND-SMITH SPECTRA

TEMPERATURE (keV)	0.5–2.0 keV			0.5–10.0 keV		
	c	*b*	*a*	*c*	*b*	*a*
1	...	...	...	0.98976	−0.693811	0.589274
2	0.98006	−0.111214	0.074738	0.74183	0.168149	0.076622
3	1.07562	−0.172770	0.045052	0.78837	0.169155	0.029814
4	1.14437	−0.238201	0.041994	0.85558	0.106416	0.021304
5	1.19418	−0.290640	0.044047	0.91672	0.040785	0.021762
6	1.23139	−0.331765	0.047111	0.96909	−0.018076	0.024729
7	1.25583	−0.359344	0.049642	1.01385	−0.068723	0.028104
8	1.27631	−0.383054	0.052145	1.05094	−0.111368	0.031331
9	1.29229	−0.401918	0.054310	1.08256	−0.147891	0.034250
10	1.30579	−0.418036	0.056253	1.10903	−0.178722	0.036790
11	1.31657	−0.430874	0.057859	1.13138	−0.204740	0.038903
12	1.32727	−0.443794	0.059521	1.15220	−0.229466	0.041146

vignetting effects (§ 4.9) forces us to break this total area up into five bins when creating mock cluster catalogs. These bins correspond to the five adopted off-axis annuli, which cover 4.3%, 13.1%, 21.7%, 30.4%, and 30.2% of the total area, respectively.

The EPIC field of view covers a 30′ diameter circle, and the CCD arrangement of the pn camera provides an active area of 649 arcmin^2. If EPIC operates for the full 10 yr of the *XMM* design lifetime and *XMM* makes an average of three pointings day^{-1}, then the total area imaged by EPIC will be $\simeq$2000 deg^2. (Although the average exposure time of the 760 GTO pointings is 22.3 ks, or 3.9 pointings day^{-1}, overheads, such as the $\sim$5 ks telescope settling time, mean that three pointings day^{-1} is a more realistic estimate.) Unfortunately, not all of the $\simeq$2000 deg^2 will be available for building serendipitous cluster catalogs. Experience from *ROSAT* suggests that only $\sim$40% of pointings are likely to be suitable, the rest being either at low Galactic latitude, overlapping previously studied fields, or have pointing targets extending over most of the field of view. Therefore, we estimate that the XCS will cover $\simeq$800 deg^2.

TABLE 2

CONVERSION FACTORS BETWEEN OBSERVED AND PSEUDOBOLOMETRIC LUMINOSITY FOR RAYMOND-SMITH SPECTRA

Temperature (keV)	0.5–10.0 keV	0.5–2.0 keV
1	1.75287	2.00900
2	1.48716	2.37600
3	1.36920	2.69564
4	1.33470	3.04131
5	1.33501	3.38720
6	1.35271	3.72926
7	1.38674	4.04849
8	1.42370	4.36129
9	1.46514	4.66436
10	1.50744	4.95957
11	1.55192	5.24149
12	1.59530	5.53199

5. SIMULATION RESULTS

The mechanisms outlined in § 4 allow us to simulate the sensitivity of the XCS in terms of both cluster detection (§ 5.1) and temperature estimation (§ 5.2). The results of these simulations, when combined with the Press-Schechter predictions described in § 3, allow us to predict the properties of the XCS (§ 5.3).

5.1. *Calculation of Sensitivity Limits for Detection*

As stated in § 4.2, our criterion for source detection is that it should be made with count statistics significant at the 8 σ level at least, so that it is possible to determine whether the source is extended or not. For the XCS predictions, we have calculated the bolometric luminosity that would yield an 8 σ detection ($L_{8\,\sigma}$) for each of 144,000 different parameter combinations. These 144,000 combinations are comprised of three cosmologies (§ 3), 12 temperatures (1 keV $< T <$ 12 keV in 1 keV increments), 40 redshifts ($0.05 < z < 2$ in $\Delta z = 0.05$ increments), five off-axis angles ($\bar{\theta} = 1\farcm5$, $4\farcm5$, $7\farcm5$, $10\farcm5$, and $13\farcm5$; § 4.9), and 20 exposure times (5 km $< t <$ 100 ks in 5 ks increments).

We determine the 144,000 $L_{8\,\sigma}$ values iteratively as follows. For a particular Ω_0, Ω_Λ, T, z, θ, and t combination, we start by calculating the half-flux radius, r_{50} (§ 4.3), in arcminutes for a given input r_c value ($r_{50} = \sqrt{3} r_c$; § 4.4). Next, we calculate the total number of background counts, N, (§§ 4.7 and 4.8) that would fall in a circle of radius r_{50} in the exposure time t (where N takes into account the effects of vignetting on the cosmic background at off-axis angle θ). Once N is known, we can calculate the number of cluster counts, S, that would need to fall inside r_{50} to yield S/N > 8.

TABLE 3

DISTRIBUTION OF *XMM* EXPOSURE TIMES IN THE GTO AND AO1 OBSERVING CYCLES

OBSERVING CYCLE	DISTRIBUTION (%)										
	5–10 ks	10–15 ks	15–20 ks	20–25 ks	25–30 ks	30–35 ks	35–40 ks	40–45 ks	45–50 ks	50–55 ks	55–100 ks
GTO	23.16	18.03	7.63	17.50	4.87	6.58	1.45	7.24	1.58	6.58	5.39
AO1	23.79	18.97	4.41	18.81	5.56	9.08	1.31	4.66	0.57	7.23	5.56

By multiplying S by $2/t$, we obtain the corresponding total count rate (where the factor of 2 accounts for those photons lying outside the r_{50} radius and the factor of $1/t$ converts from total counts to a count rate). This count rate can then be converted into a flux by dividing by the appropriate vignetting factor (§ 4.9) and then multiplying by the appropriate count rate to flux-conversion factor (§ 4.6). Using the appropriate K-correction (§ 4.13), we calculate the corresponding (0.5–2.0 keV) luminosity. We compare this luminosity to the one obtained from equation (3) using the input value of r_c. If the two luminosities differ by more than 20%, we recalculate r_c and repeat the whole procedure. We always start the iteration with $r_c = 250$ kpc. Usually the process converges after only one or two adjustments to r_c. After convergence, we define $L_{8\,\sigma}$ using the appropriate bolometric correction (§ 4.13).

We note that, across all 144,000 calculations, the smallest r_{50} value used to derive an $L_{8\,\sigma}$ value was $\simeq 20''$. To confirm that clusters of this size, and larger, will be flagged as extended sources, we have computed, using QUICKSIM, how the radius enclosing half the flux in a model *XMM* point-spread function varies with off-axis angle. We find that the maximum size of this radius is only $\simeq 13''$. Therefore, it follows that all clusters detected at greater than 8 σ will be flagged as extended sources; i.e., the completeness of the XCS should not suffer by the imposition of an extent criterion.

It would be impractical to provide tables listing the results of all 144,000 calculations, so instead we give a few illustrative examples. These following examples are based on calculations in the first radial bin ($\bar{\theta} = 1.'5$) and in an $\Omega_0 = 1, \Omega_\Lambda = 0$ cosmology:

1. The highest number of counts required inside r_{50} for an 8 σ detection was 255, arising for a cluster at redshift $z = 2$ with a temperature $T = 1$ keV, observed for 100 ks. Such a cluster would have a total count rate of 0.0051 count s^{-1}, a flux of 7.06×10^{-15} ergs s^{-1} cm^{-2}, and a luminosity of 7.48×10^{44} ergs s^{-1}.
2. The lowest number of counts required inside r_{50} for an 8 σ detection was 77, arising for a cluster at redshift $z = 0.35$ with a temperature of $T = 12$ keV, observed for 5 ks. Such a cluster would have a total count rate of 0.0308 count s^{-1}, a flux of 3.11×10^{-14} ergs s^{-1} cm^{-2}, and a luminosity of 0.16×10^{44} ergs s^{-1}.
3. All clusters lying at $z \lesssim 1.5$ that are brighter than L_* will be detected at greater than 8 σ in a 5 ks pointing. At $z = 1.5$ an L_* cluster has a flux of 4.24×10^{-14} ergs s^{-1} cm^{-2}. Here we assume that L_*, the "knee" in the Schechter function fitted to the X-ray cluster luminosity function, has a value of 4.8×10^{44} ergs s^{-1}; this is the average of the values found by De Grandi et al. (1999b) and Ebeling et al. (1998). Such a cluster has a temperature of 5.5 keV based on the L_X-T relation of AF98, equation (1).
4. In the average exposure time (22.3 ks; § 4.14) of the 760 GTO pointings, it will be possible to detect clusters brighter than 2.4×10^{44} ergs s^{-1} (i.e., $0.5 \times L_*$) out to redshifts of $z \simeq 1.6$. (Such a cluster has a temperature of 3.7 keV based on the L_X-T relation of AF98.)

5.2. *Calculation of Sensitivity Limits for Temperature Estimation*

The EPIC-pn camera is able to estimate the energies of all incident photons, so it can perform low-resolution spectroscopy as well as broadband imaging. This means that we are able to estimate temperatures for the clusters we detect, provided the signal-to-noise ratio of the source spectrum is sufficiently high. This is clearly a great advantage, since, for those clusters for which it is possible, we shall not need to obtain follow-up observations to determine their temperature. Cluster-temperature measurements are important for cosmological-parameter estimation, since T is more readily related to cluster mass (in terms of which theoretical predictions are made) than is (the more easily measured) X-ray luminosity.

To assess the extent to which we will be able to take advantage of the *XMM* spectral resolution, we have calculated the minimum bolometric luminosity (L_T) that would yield a temperature estimate for each of our 144,000 parameter combinations. We stress that, in most cases, determination of the redshift of the cluster will be required before its temperature can be estimated. This remains true even for spectra of high signal-to-noise ratio, owing to the degeneracy between temperature and redshift in the spectral fitting when thermal bremsstrahlung is the dominant emission process. However, if there is significant line emission in addition to the bremsstrahlung radiation (which is especially true for low-temperature, high-metallicity plasmas), it is sometimes possible to measure the redshifts from emission features such as the 7 keV Fe line. R. F. Mushotzky (1994, private communication) and others have shown that this technique works, and we certainly will apply it where possible to XCS data. Alternatively, we might also expect to be able to obtain crude redshift estimates using the measured flux and extent; this method is cosmology-dependent but is still worthy of further investigation.

Given that the redshift will be known prior to the spectral fitting, it will be possible to choose the metric aperture size most suitable for temperature measurements for each cluster. To reflect this, we allow the radius of apertures used in our temperature-sensitivity–limit calculations to vary (with the constraint that it must never be smaller than r_{50}) so as to include the maximum number of photons but without being swamped by the background. (This is in contrast to our detection-sensitivity calculations, for which we always used r_{50}, since the detection software will most likely only pick out the central $\simeq 50\%$ of the cluster flux; see § 4.3.) We also set the additional criteria that the number of background counts in the aperture must never exceed the number of cluster counts and that the cluster counts must never be less than 1000. The aperture sizes thus chosen varied from r_{50} to r_{89}, and the number of background counts inside these apertures varied from $\simeq 250$ to $\simeq 1500$ (with an average value of $\simeq 600$).

The accuracy to which temperatures can be estimated depends on three factors: the cluster redshift, the cluster temperature, and the signal-to-noise ratio of the spectrum. We illustrate this via Figure 4, which shows the input versus fitted temperatures for representative values of the cluster redshift, cluster temperature, and background count rate. For this figure, we created, and then fitted, 20 fake spectra (with $n_H = 4 \times 10^{20}$ cm^{-2} and $Z = 0.3\ Z_\odot$) for each of the listed temperature-redshift–background combinations using the XSPEC commands FAKEIT and FIT, respectively. The mean and standard deviation of the 20 fits are plotted in Figure 4. These fits were all performed on spectra containing 1000 counts because only about 1% of the 144,000 L_T calculations produced background counts—and

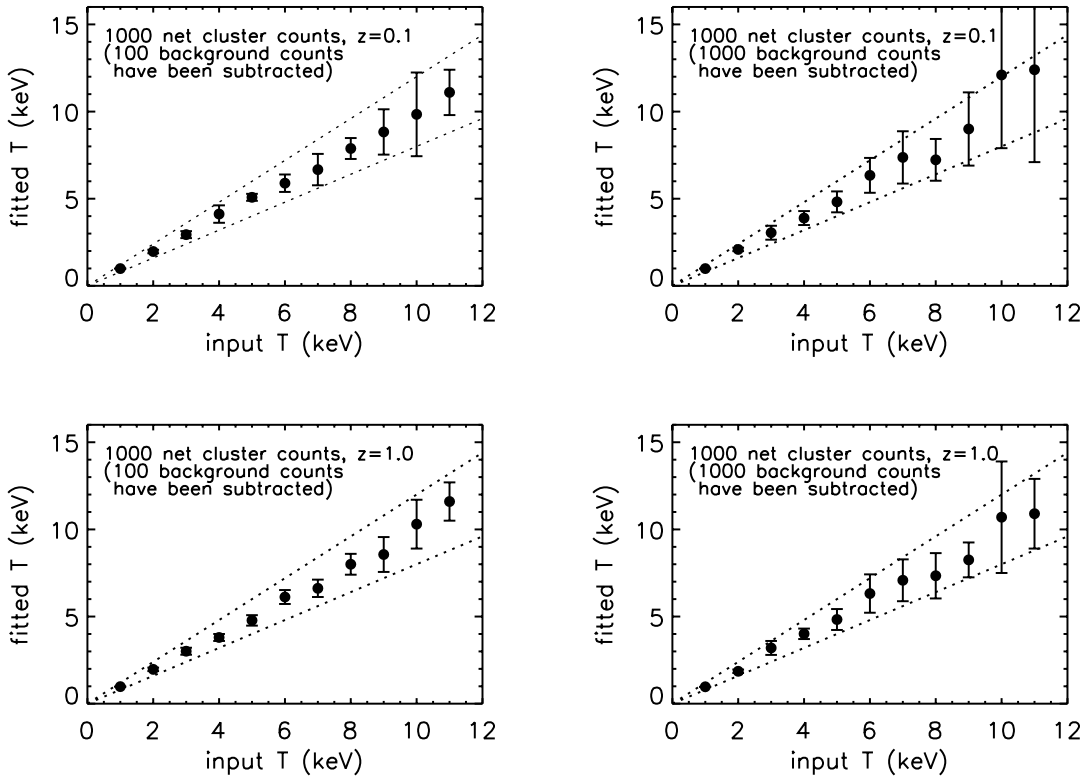

FIG. 4.—Fitted temperatures vs. input temperatures for four different combinations of redshift and background contamination. All spectra were created using FAKEIT in XSPEC. The dotted lines show input temperature plus (*upper line*) and minus (*lower line*) 20%.

hence cluster counts—that exceeded 1000. From the figure, it is clear that a spectrum of 1000 counts will yield temperature estimates of varying accuracies, with the most accurate values being derived for the lowest temperature systems. The lowest accuracy results will come from high-temperature clusters at low redshift with high background count rates. We note that the accuracy improves with redshift for high-temperature systems because the "knee" in the thermal bremsstrahlung spectrum moves to lower energies, where *XMM* has more effective area.

Some examples of our temperature sensitivity limits are as follows (assuming $\bar{\theta} = 1'.5$, $\Omega_0 = 1$, and $\Omega_\Lambda = 0$): Cool clusters ($T = 2$ keV) will yield temperature measurements only out to $z \simeq 0.21$ in 5 ks exposures. Even in a 100 ks exposure, the maximum redshift for temperature determination for $T = 2$ keV clusters stretches only to $z \sim 0.72$. (Based on the AF98 L_X-T relation, we expect a $T = 2$ keV cluster to have a luminosity of $\simeq 0.7 \times 10^{44}$ ergs s^{-1}.) By contrast, hotter clusters, which are brighter, yield temperature measurements to higher redshifts. For example, temperatures will be measured for $L_X > L_*$ ($T > 5.5$ keV) clusters to $z \sim 0.6$ (1.1, 2.0) in 5 (22.3, 100) ks exposures.

5.3. *Expected Catalog Properties*

In §§ 5.1 and 5.2 we computed the luminosity threshold for cluster detection ($L_{8\,\sigma}$) and temperature estimation (L_T), respectively, for 144,000 different combinations of Ω_0, Ω_Λ, T, z, θ, and t. Combining these luminosity thresholds with the results of § 3 allows us to estimate how many clusters will be included in our catalog (and for how many of them we can estimate a temperature). We note that when doing so we assume that clusters are randomly located on the sky, that the total areal coverage is 800 deg^2 (§ 4.14) and that the pointing exposure times are distributed according to Table 3. The results of our catalog predictions are summarized in Table 4 and Figures 5 and 6.

The XCS will not have a single, well-defined flux limit because it will be made up of pointings with a wide dispersion of exposure times (§ 4.14) and because—in the *XMM* band at least—count rate to flux-conversion factors are a complex function of z and T (§ 4.6) and θ (§ 4.9). Despite this, we have been able to estimate an effective flux limit for the survey by comparing the numbers of expected $z > 0$ cluster detections (as listed in the first line of Table 4; 8300, 750, 61, etc.) with the $N(f)$ values in Figure 1 (after appropriate scaling from 4π sr to 800 deg^2). Doing so provides nine estimates of the survey flux limit, all of which turn out to be close to 1.5×10^{-14} ergs s^{-1} cm^{-2}. Repeating the procedure for the $z < 0.3$ and $z > 1.0$ (by comparison with Figs. 2 and 3, respectively) also yields flux limits of $\simeq 1.5 \times 10^{-14}$ ergs s^{-1} cm^{-2}. We conclude, therefore, that the effective XCS flux limit will be $\simeq 1.5 \times 10^{-14}$ ergs s^{-1} cm^{-2} but stress that individual pointings in the survey will have flux limits that may be higher or lower than this value.

In § 3 we noted that any survey that reaches a flux limit of $\sim 1 \times 10^{-14}$ ergs s^{-1} cm^{-2} will be able to detect almost all the $T > 4$ keV clusters in its survey region irrespective of redshift. This is supported by Figure 5, which shows the integral redshift distributions, $N(z)$, predicted for the XCS in the three cosmologies we consider. The total number of clusters (as predicted by Press-Schechter theory) are depicted by solid curves, whereas the number of expected XCS detections are depicted by dashed curves. For $T > 6$ keV clusters (*top panel*) the two curves are coincident out to

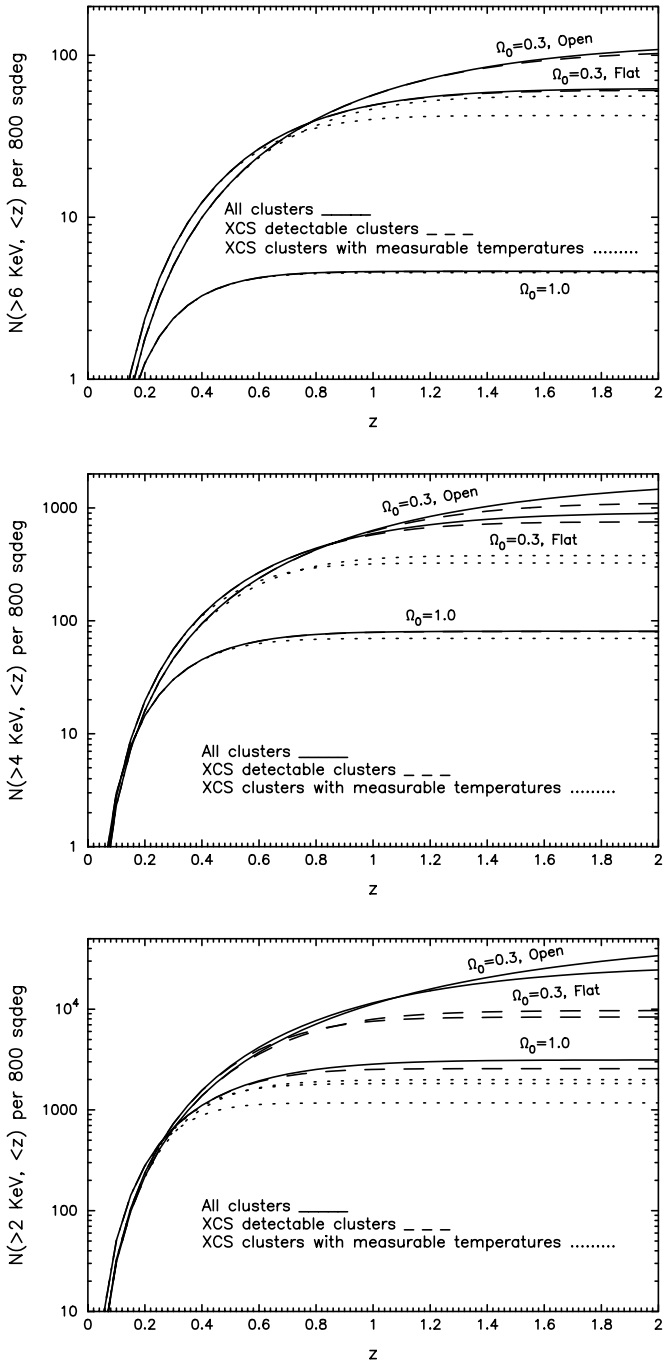

FIG. 5.—Cumulative redshift distribution, $N(<z)$, of galaxy clusters per 800 deg^2 with X-ray temperature in excess of 6 keV (*upper panel*), 4 keV (*middle panel*), and 2 keV (*lower panel*). The solid lines show the result one would obtain if there was no limitation on the detectable flux. The dashed and dotted lines show our predictions for the XCS, where the dashed line represents the expected number of greater than 8 σ detections, and the dotted line represents the expected number of clusters bright enough to allow temperature measurements.

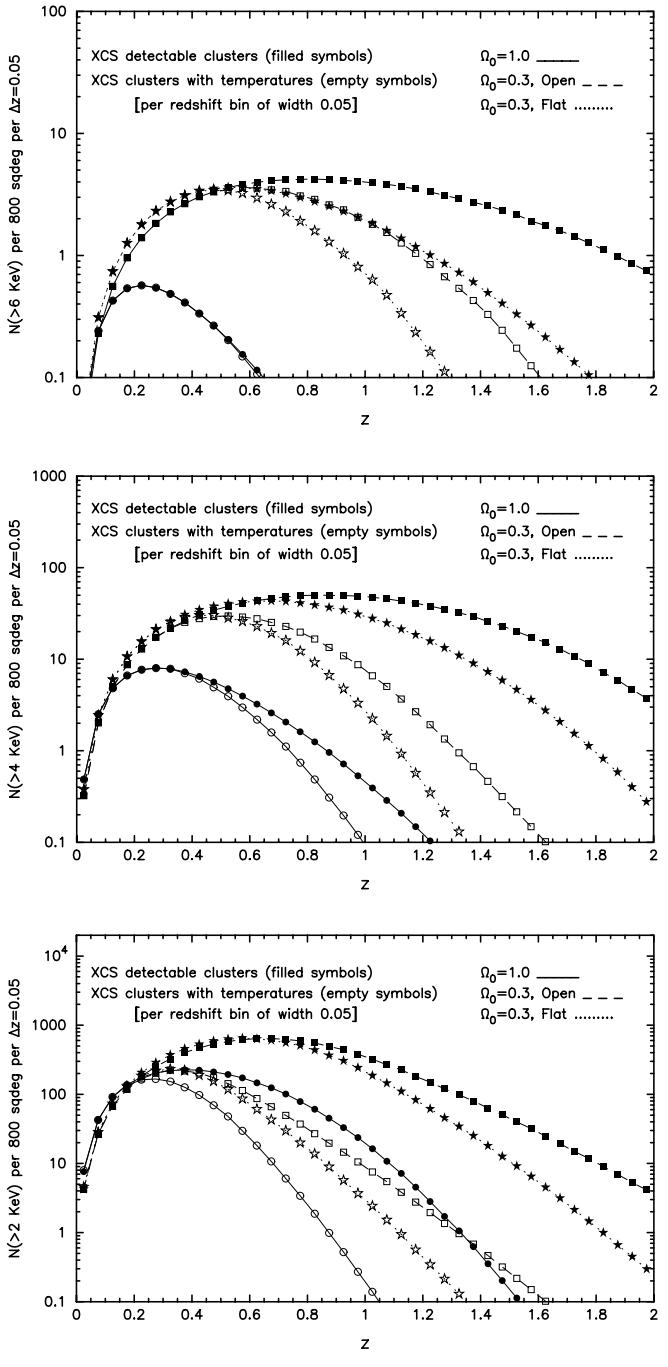

FIG. 6.—Predicted redshift distributions (evaluated in bins of width $\Delta z = 0.05$) corresponding to the cumulative counts of Fig. 5. The filled and empty symbols denote clusters detected and with temperatures estimated, respectively, in the three cosmological models: Einstein–de Sitter (*solid line*), low-density open (*dashed line*), and low-density flat (*dotted line*).

$z \simeq 1.4$, meaning that we can expect to detect all $T > 6$ keV clusters at $z < 1.4$. From the middle panel, we can see that incompleteness sets in earlier for the $T > 4$ keV clusters, but even so we can expect to detect almost all $T > 4$ keV clusters out to at least $z \simeq 1$. By contrast, we expect to be incomplete in terms of $T > 2$ keV clusters by $z \simeq 0.5$, and, by $z \simeq 2$, we can expect to be detecting only 20% of the $T > 2$ keV clusters (if $\Omega_0 = 0.3$) in our survey region.

Also shown on Figure 5 are our predictions for the number of clusters that we will detect with sufficient signal-to-noise ratio to be able to estimate temperatures (*dotted curves*). These numbers are also given in parentheses in Table 4. We will obtain temperatures for all $T > 6$, $T > 4$, and $T > 2$ keV clusters out to $z \simeq 0.7$, $z \simeq 0.5$, and $z \simeq 0.3$, respectively. To further illustrate the expected properties of the XCS, we plot in Figure 6 the differential redshift distribution as a function of cosmology and temperature. This figure shows how many clusters will be detected in each $\Delta z = 0.05$ bin when $\Omega_0 = 1$ (*solid lines*, *squares*), $\Omega_0 =$

TABLE 4

EXPECTED NUMBER OF CLUSTERS DETECTED IN AN *XMM* SERENDIPITOUS SURVEY FOR THREE COSMOLOGICAL MODELS

z	$T>2$	$T>4$	$T>6$
	$\Omega_0=0.3$, $\Omega_\Lambda=0.7$		
>0.....	8300 (1800)	750 (320)	61 (42)
>0.3.....	7600 (1200)	700 (270)	54 (36)
>1.....	750 (6)	170 (6)	12 (2)
	$\Omega_0=1.0$, $\Omega_\Lambda=0.0$		
>0.....	2600 (1200)	80 (70)	5 (5)
>0.3.....	1900 (570)	50 (40)	2 (2)
>1.....	46 (0)	1 (0)	0 (0)
	$\Omega_0=0.3$, $\Omega_\Lambda=0.0$		
>0.....	9700 (2000)	1100 (380)	110 (56)
>0.3.....	9000 (1400)	1100 (330)	100 (51)
>1.....	1700 (26)	480 (24)	50 (9)

NOTE.— Survey covers 800 deg^2. The main numbers are for detections, while the numbers in parentheses are detections with sufficient flux to yield temperatures.

0.3, $\Omega_\Lambda = 0$ (*dashed lines*, *stars*), and $\Omega_0 = 0.3$, $\Omega_\Lambda = 0.7$ (*dotted lines*, *circles*). In order to differentiate between curves representing the number of detections and curves representing the number of clusters with temperature estimates, we have used solid and open symbols, respectively.

6. DISCUSSION AND CONCLUSIONS

A cluster catalog of the quality described in § 5.3 would have a great many uses. Here we describe briefly a subset of these to give a feel for the kind of science that the XCS will make possible. We also discuss some caveats relating to the methods used herein and present our conclusions.

6.1. *Science from the Catalog*

The science that can be derived from the XCS can be loosely divided into two categories: science that can be obtained directly from the catalog itself (for the most part assuming that follow-up observations have provided cluster redshifts and enabled temperature determination where possible) and those future projects that can build on the XCS data. We give a few examples of both sorts of project here.

6.1.1. *Constraints on Cosmological Parameters*

The XCS cluster temperature and redshift distributions can be used as a direct probe of the cosmological parameters Ω_0 and Ω_Λ. The survey's size, redshift distribution, and selection criteria are ideally suited to this task. The XCS will provide stringent constraints on Ω_0 and has the potential to offer the first constraint on Ω_Λ from cluster number density evolution. The power of the XCS to constrain these parameters is clearly demonstrated in Figure 5, from which it is apparent that there is about an order-of-magnitude difference between the number of high-temperature ($T > 4$ keV) clusters in the $\Omega_0 = 1$ case compared to either of the two $\Omega_0 = 0.3$ cases. At lower temperatures ($T > 2$ keV) the differences between the various models are less apparent, demonstrating that it is important to concentrate on the high-temperature systems when attempting to measure cosmological parameters.

It is beyond the scope of this paper to make detailed predictions of the errors on Ω_0 that would result from the XCS. To do so would require a careful tracking of the theoretical uncertainties in the number density predictions, especially those connected with the amplitude of the power spectrum, and ideally would also take into account the weak sensitivity of the predictions to quantities such as the power spectrum shape. Further, the modeling of the observational errors, and in particular the cosmic variance contribution—which assesses the extent to which the observations might be a statistical fluke—is a subtle business requiring detailed Monte Carlo and probably N-body simulations. The former can only be carried out in detail once the true distribution of observing times and the fraction of usable pointings is known. It may also prove necessary to model evolution in the temperature-luminosity relation (§ 6.1.2). (It is for these reasons that we are unable to add error bars to the predictions in Figs. 1–6.)

In order to go beyond measurements of Ω_0 and start to constrain Ω_Λ, one must study the $z > 1$ population; from Figure 6 we can see that there is little difference between the cluster number density evolution predictions for the two $\Omega_0 = 0.3$ cosmologies below $z = 1$. But, for $z > 1$, the number density of galaxy clusters for $\Omega_0 = 0.3$ in open models is more than twice that in flat models. Once all the $z > 1$ clusters detected have measured redshifts and temperatures, it should be possible to constrain Ω_Λ. However, in view of the modeling uncertainties described above, it is premature to try and assess how well that can be done, since this will only become apparent when the actual data are available.

It is important to note that the cosmological constraints derived from the XCS will be important even in the era of sensitive cosmic microwave background (CMB) anisotropy experiments such as *Planck* because the cluster measurements can help to break degeneracies in cosmological parameters inherent in CMB analyses. Since the microwave anisotropy is expressed in terms of angular scales on the sky, the cosmological parameters Ω_0 and Ω_Λ are constrained only in the combination in which they arise in the angular diameter distance at the redshift of the last scattering surface—i.e., such observations can only constrain the universe to lie somewhere along a line in the (Ω_0, Ω_Λ) parameter space rather than at a single point. This degeneracy can be broken, in principle, in two ways. On the very largest angular scales it is weakly broken by the integrated part of the Sachs-Wolfe effect, but these low-order multipoles suffer a large "cosmic variance" that limits the accuracy with which they can be estimated. On small angular scales, it is mildly broken by gravitational lensing effects. Both these effects are small, and it is expected that the degeneracy largely still will be present even after *Planck* has flown (Bond, Efstathiou, & Tegmark 1997). One therefore requires other types of observations to break the degeneracy. (See Bahcall et al. 1999 for an overview of how different methods can be used in combination to constrain cosmological parameters.) The sorts of measurements that can be used to break the CMB Ω_0-Ω_Λ degeneracy include cluster number density evolution, large-scale structure analyses, and the magnitude-redshift relation for Type Ia supernovae (Perlmutter et al. 1999). Because each of these methods has intrinsic biases, it is important to pursue all of them to as high an accuracy as possible in order to derive a consistent model of the universe.

6.1.2. *Evolution of X-Ray Properties*

The XCS will greatly improve our understanding of how cluster properties, such as luminosity, temperature, metallicity, gas mass fraction, core radius, etc., evolve. Importantly, it will allow the luminosity-temperature relation to be measured in a coherent fashion over a wide redshift range. The quantification of L_X-T evolution is crucial to our ambition to measure cosmological parameters from cluster number densities. From Table 4, we can see that the XCS will yield temperature measurements for 1800 clusters with $T > 2$ keV in the low-density flat cosmology. These measurements will yield the most accurate derivation of the L_X-T relation to date. Not only will the derivation include a great many more clusters, but, for the first time, these clusters will have been drawn from a single, statistically complete sample.

6.1.3. *Gravitational Lensing by XCS Clusters*

X-ray clusters magnify background galaxies via gravitational lensing. This effect is well known at optical wavelengths (e.g., Luppino et al. 1999), but, as shown by Smail, Ivison, & Blain (1997), it is particularly exciting in the submillimeter. Here, the combination of the lensing amplification and the positive K-correction in the submillimeter (resulting from the sharp decline in the spectral energy distribution of starburst galaxies longward of ~ 100 μm) means that such galaxies can be readily detected to extremely high redshift ($z > 5$). The follow-up of lensed galaxies around XCS clusters with the coming generation of (sub)millimeter instruments, such as the Atacama Large Millimeter Array, will provide an important insight into the star-formation history of the universe. Lensing signals can also be used to measure total masses and mass profiles of clusters in a manner complementary to X-ray methods (e.g., Squires et al. 1997).

6.1.4. *Sunyaev-Zeldovich Follow-up*

The Sunyaev-Zeldovich (SZ) effect (Sunyaev & Zeldovich 1972) describes the inverse Compton scattering of CMB photons to higher energies via interactions with hot electrons in the ICM. Measurements of the SZ effect, in combination with X-ray observations, provide a useful cosmological tool. They can be used to constrain the value of the Hubble parameter (H_0; e.g., Birkinshaw 1999), the universal baryon fraction (e.g., Grego 1998), cluster peculiar velocities (e.g., Holzapfel et al. 1997), and have the potential to place powerful constraints on the value of Ω_0 (e.g., Bartlett, Blanchard, & Barbosa 1998). Therefore, SZ follow-up of XCS clusters will yield many important results, the most obvious of which would be the measurement of H_0 as a function of redshift. This $H_0(z)$ measurement would take advantage of the large number of high-z clusters in the XCS and of the fact that the SZ effect is redshift independent. The XCS also has the potential to provide the required X-ray follow-up for blind SZ-surveys (such as that proposed by Holder et al. 2000). These blind surveys hope to take advantage of the redshift independence of the SZ effect in order to detect very distant clusters.

6.1.5. *Analysis of CMB Foregrounds*

The limit to which the *Microwave Anistropy Probe* and *Planck* satellites can determine the power spectrum of CMB anisotropies on small scales is likely to be set by the effectiveness of the foreground analyses. One of the major sources of CMB foreground confusion is the SZ signal from X-ray clusters of galaxies. Since the SZ effect is approximately redshift independent, clusters at all distances will contribute to the foreground signal. In a low-density cosmology, the mean SZ signal comes from a broad range of redshifts out to $z \simeq 2$ (da Silva et al. 2000). The XCS will play a crucial role in the understanding of this signal because it will provide a statistical description of the cluster population out to high redshifts. Moreover, in the regions covered by the XCS, it will be possible to mask out the signal from individual clusters from the CMB maps.

6.2. *Limitations of Our Calculations*

As detailed in § 4, our simulations rest on a set of assumptions and simplifications, which were chosen because they all seem reasonable given current knowledge. There are, however, some limitations to the accuracy with which we can predict expectations for the XCS, and we discuss some of them below.

6.2.1. *Contamination by Low-Mass Groups*

The application of an extent criterion will not be sufficient to remove all the contamination in the cluster candidate list. Low-mass groups (including "fossil groups"; Ponman et al. 1994; Vikhlinin et al. 1999; Romer et al. 2000) and some very low redshift galaxies will also enter the list by virtue of their extent. Low-mass (and hence low-temperature) groups are certainly interesting objects; they provide invaluable insight into the processes of elliptical-galaxy evolution, metal enrichment in the intracluster medium, and the dynamics of extended dark halos (Mulchaey & Zabludoff 1999). However, they have a very limited role to play in the derivation of Ω_0 and Ω_Λ (because of the increasing degeneracy between models as the temperature limit is decreased; see Fig. 5). The Press-Schechter formalism becomes unreliable below $T \simeq 2$ keV, so we are not able to predict the number of $T < 2$ keV groups that will be detected by the XCS. For typical values of the temperature and bolometric luminosity of the intragroup medium ($T = 1$ keV, $L_X = 10^{42}$ ergs s^{-1}; Mulchaey & Zabludoff 1999), we have estimated the maximum redshift at which a group would be detected by our survey to be $z \sim 0.05$ (0.09, 0.17) in 5 (22.3, 100) ks. We are actively investigating ways to flag potential $T < 2$ keV objects using a combination of extent, *XMM* spectra, and cross-correlations with optical sky survey data.

6.2.2. *Contamination by Point-Source Emission*

We assume in § 5.3 that every cluster we detect at greater than 8 σ will be included in the final XCS cluster catalog, but this may not always be the case. Some clusters might be excluded if they are contaminated by point-source emission, which might originate from an active galaxy inside the cluster, a foreground object, such as an M star, or a background object, such as a quasar. Romer et al. (2000) describe the case of an extended X-ray source (RX J0947.8) that was excluded from their cluster catalog on the grounds of it being coincident with a $z = 0.63$ quasar despite there being a spectroscopically confirmed cluster at the same position and redshift. A total of four clusters were rejected from the Bright SHARC cluster catalog because the quality of the *ROSAT* data did not permit the cluster flux to be disentangled from that of a contaminating point source. Romer et al. (2000) claim that two of these systems probably have sufficient, uncontaminated flux to merit inclusion in

the Bright SHARC cluster catalog, which corresponds to an incompleteness of the whole catalog at the 5% level. We expect the incompleteness level to be much lower than this for the XCS since the improved spatial resolution of *XMM* over *ROSAT* will significantly enhance our ability to mask out point-source contamination when measuring cluster fluxes. We expect therefore that the wrongful exclusion of clusters from the XCS catalog will occur only very rarely and have an insignificant effect on our ability to use the XCS as a cosmological tool.

6.2.3. *Effect of Assumptions about the Cluster Model*

Perhaps the greatest uncertainty in our calculations comes from the simplified model of the distribution and state of the intracluster medium we employed. Our use of the isothermal β-model was justified in part by the results of Mohr et al. (1999), who showed that it well described the azimuthally averaged properties of known clusters. However, this work was carried out in the *ROSAT* bandpass (0.5–2.0 keV), over which the emissivity of the X-ray gas is almost insensitive to cluster temperature for $T \gtrsim 2$ keV. And, as emphasized recently by Ettori (1999a), the assumption of a simple isothermal β-model will lead to significant errors when a cluster with a significant temperature gradient is observed in a broadband bracketing the energy corresponding to its mean temperature. Evidence to suggest that the cluster gas is not isothermal comes from spatially resolved cluster-temperature maps (e.g., Markevitch et al. 1998) and from the so-called β-discrepancy (e.g., Sarazin 1988; Bahcall & Lubin 1994), which describes the fact that fitted values of β are not consistent with the values expected from the combination of cluster temperatures with galaxy velocity dispersions.

We have also ignored the effect of cooling flows in the cluster core. A significant fraction of relaxed clusters have regions of cool, dense gas in their cores (e.g., AF98), and, as Ettori (2000b) has pointed out, a modified version of equation (2) would be more appropriate to describe such clusters.

More fundamentally, it is possible, of course, that the clusters we detect at high redshift will not be virialized systems. Clusters in the process of formation may have significant nonthermal components to their X-ray luminosities, for example, from shocks resulting from subcluster merging. A classic example of such a cluster is RX J0152.7 (Ebeling et al. 2000; Romer et al. 2000), which has a high total luminosity (8.26×10^{44} ergs s^{-1}, $z = 0.83$) but is made up of at least two components. It is not possible to predict, at this stage, what the net effect of unvirialized systems will be on the properties of the XCS, but the spatial and spectral resolution of EPIC should help us to recognize such systems. The XCS may even show that clusters are *not* suitable as cosmological probes above a certain redshift; indeed, perhaps effects such as these lie behind the detection to date of a (possibly) surprisingly large number of massive clusters at high redshift (Luppino & Gioia 1995; Donahue 1996; Luppino & Kaiser 1997; Donahue et al. 1998; Eke et al. 1998), which has been claimed to be troublesome for conventional models of structure formation.

6.3. *Conclusions*

We have predicted the expected properties of a serendipitous cluster survey based on archival *XMM* pointing data. We have done this using simulations that combine a theoretical model of the properties of the cluster population, as a function of cosmology, with a detailed description of the characteristics of the EPIC camera and a generic model for cluster surface brightness profiles. We have shown that the catalog that would result from such a survey will surpass existing catalogs of high-redshift ($z > 0.3$) clusters in size, quality, and redshift coverage, while at low redshifts ($z < 0.3$) the catalog will yield many more cluster-temperature measurements than have ever been measured before.

It is clear that while the methods presented here may be adequate to yield reasonably realistic predictions for what we can expect to get from the XCS, the actual analysis of the data from the survey will require a more sophisticated approach, informed by detailed physical models resulting from pointed observations of individual clusters made by *Chandra* and *XMM* itself. This must, however, be tempered by the requirement that the final set of cluster selection criteria be readily modeled by Monte Carlo methods; the XCS will have its greatest impact in statistical analyses, so it must be constructed in such a way that its selection function can be well understood.

We thank M. Watson, G. Stewart, J. Osborne, B. Nichol, and C. Collins for a series of useful discussions. We also thank M. Arnaud for her assistance with the cosmic-background spectrum. A. K. R. acknowledges financial support from the CMU physics department and NASA grant NAG 5-7926. P. T. P. V. was supported by the PRAXIS XXI program of FCT (Portugal), and R. G. M. acknowledges support from PPARC. Finally, we thank our ApJ editor (J. Huchra) and an anonymous referee for their helpful comments.

REFERENCES

Abell, G. O. 1958, ApJS, 3, 211
Abell, G. O., Corwin, H. G., & Olowin, R. P. 1989, ApJS, 70, 1
Allen, S. W., & Fabian, A. C. 1998, MNRAS, 297, L57 (AF98)
Arnaud, K. A. 1996, ASP Conf. Ser. 101, Astronomical Data Analysis and Software Systems V, ed. G. H. Jacoby & J. Barnes (San Francisco: ASP), 17
Arnaud, M., & Evrard, A. E. 1999, MNRAS, 305, 631
Bahcall, N. A., & Fan, X. 1998, ApJ, 504, 1
Bahcall, N. A., & Lubin, L. M. 1994, ApJ, 426, 513
Bahcall, N. A., Ostriker, J. P., Perlmutter, S., & Steinhardt, P. J. 1999, Science, 284, 1481
Bartlett, J. G., Blanchard, A., & Barbosa, D. 1998, A&A, 336, 425
Birkinshaw, M. 1999, Phys. Rep., 310, 97
Blanchard, A., Sadat, R., Bartlett, J. G., & Le Dour, M. 2000, A&A, 362, 809
Bludman, S. A. 1998, ApJ, 508, 535
Böhringer H., et al. 1998, in Proc. 14th IAP Conf., Wide Field Surveys in Cosmology, ed. S. Colombi, Y. Mellier, & B. Raban (Paris: Editions Frontières), 261
Bond, J. R., Efstathiou, G., & Tegmark, M. 1997, MNRAS, 291, L33
Borgani, S., Rosati, P., Tozzi, P., & Norman, C. 1999, ApJ, 517, 40
Bryan, G. L., & Norman, M. L. 1998, ApJ, 495, 80
Castander, F. J., et al. 1995, Nature, 377, 39
Chen, L.-W., Fabian, A. C., & Gendreau, K. C. 1997, MNRAS, 285, 449
Colberg, J. M. et al. 1998, in Proc. 14th IAP Conf., Wide Field Surveys in Cosmology, ed. S. Colombi, Y. Mellier, & B. Raban (Paris: Editions Frontières), 247
Collins, C. A., Burke, D. J., Romer, A. K., Sharples, R. M., & Nichol R. C. 1997, ApJ, 479, L117
Dalton, G. B., Efstathiou, G., Maddox, S. J., & Sutherland, W. J. 1992, ApJ, 390, L1

da Silva, A. C., Barbosa, D., Liddle, A. R., & Thomas, P. A. 2000, MNRAS, 317, 37
De Grandi, S., et al. 1999a, ApJ, 514, 148
———. 1999b, ApJ, 513, L17
Donahue, M. 1996, ApJ, 468, 79
Donahue, M., & Voit, G. M. 1999, ApJ, 523, L137
Donahue, M., Voit, G. M., Gioia, I., Luppino, G., Hughes, J. P., & Stocke, J. T. 1998, ApJ, 502, 550
Ebeling, H., Edge, A. C., Böhringer, H., Allen, S. W., Crawford, C. S., Fabian, A. C., Voges, W., & Huchra, J. P. 1998, MNRAS, 301, 881
Ebeling, H., et al. 2000, ApJ, 534, 133
Ebeling, H., Voges, W., Böhringer, H., Edge, A. C., Huchra, J. P., & Briel, U. G. 1996, MNRAS, 283, 1103
Efstathiou, G., Bond, J. R., & White, S. D. M. 1992, MNRAS, 258, 1
Eke, V. R., Cole, S., & Frenk, C. S. 1996, MNRAS, 282, 263
Eke, V. R., Cole, S., Frenk, C. S., & Henry, J. P. 1998, MNRAS, 298, 1145
Ettori, A. 2000a, MNRAS, 311, 313
———. 2000b, MNRAS, 318, 1041
Evrard, A. E. 1989, ApJ, 341, L71
Fukazawa, Y., Makishima, K., Tamura, T., Ezawa, H., Xu, H., Ikebe, Y., Kikuchi, K., & Ohashi, T. 1998, PASJ, 50, 187
Gheller, C., Pantano, O., & Moscardini, L. 1998, MNRAS, 296, 85
Gioia, I. M. 1998, in Proc. 14th IAP Conf., Wide Field Surveys in Cosmology, ed. S. Colombi, Y. Mellier, & B. Raban (Paris: Editions Frontières), 265
Gioia, I. M., Henry, J. P., Maccacaro, T., Morris, S. L., Stocke, J. T., & Wolter, A. 1990, ApJ, 356, L35
Grego, L. 1998, Ph.D. thesis, Caltech
Gunn, J. E., et al. 1998, AJ, 116, 3040
Henry, J. P. 1997, ApJ, 489, L1
———. 2000, ApJ, 534, 565
Henry, J. P., Gioia, I. M., Maccacaro, T., Morris, S. L., Stocke, J. T., & Wolter, A. 1992, ApJ, 386, 408
Henry J. P., et al. 1997, AJ, 114, 1293
Holder, G. P., Mohr, J. J., Carlstrom, J. E., Evrard, A. E., & Leitch, E. M. 2000, ApJ, 544, 629
Holzapfel, W. L., Ade, P. A. R., Church, S. E., Mauskopf, P. D., Raphaeli, Y., Wilbanks, T. M., & Lange, A. E. 1997, ApJ, 481, 35
Jones C., & Forman W. 1992, in Clusters and Superclusters of Galaxies, ed. A. C. Fabian (Dordrecht: Kluwer), 49
Jones, L. R., Scharf, C., Ebeling, H., Perlman, E., Wegner, G., Malkan, M., & Horner, D. 1998, ApJ, 495, 100
Kaastra, J. S., & Mewe, R. 1993, Legacy, 3, 16
Labov, S. E., & Bowyer, S. 1991, ApJ, 371, 810
Lumsden, S. L., Nichol, R. C., Collins, C. A., & Guzzo L. 1992, MNRAS, 258, 1
Luppino, G. A., & Gioia I. 1995, ApJ, 445, L77
Luppino, G. A., Gioia, I. M., Hammer, F., Le Fevre, O., & Annis, J. A. 1999, A&AS, 136, 117
Luppino, G. A., & Kaiser, N. 1997, ApJ, 475, 20
Mann, R. G., Peacock, J. A., & Heavens, A. F. 1998, MNRAS, 293, 209
Markevitch, M., Forman, W. R., Sarazin, C. L., & Vikhlinin, A. 1998, ApJ, 503, 77
Martinelli, A., Matteucci, F., & Colafrancesco, S. 2000, A&A, 354, 387
Mattig, W. 1958, Astron. Nachr., 284, 109
Mohr, J. J., Mathiesen, B., & Evrard, A. E. 1999, ApJ, 517, 627
Morrison, R., & McCammon, D. 1983, ApJ, 270, 119
Mulchaey, J. S., & Zabludoff, A. I. 1999, ApJ, 514, 133
Mushotzky, R. F., & Scharf, C. A. 1997, ApJ, 482, L13
Oukbir, J., & Blanchard, A. 1992, A&A, 262, L21
Peacock, J. A., & Dodds, S. J. 1994, MNRAS, 267, 1020
Pen, U.-L. 1998, ApJ, 498, 60
———. 1999, ApJS, 120, 49
Perlmutter, S., et al. 1999, ApJ, 517, 565
Ponman, T. J., Allan, D. J., Jones, L. R., Merrifield, M., McHardy, I. M., Lehto, H. J., & Luppino, G. A. 1994, Nature, 369, 462
Postman, M., Lubin, L. M., Gunn, J. E., Oke, J. B., Hoessel, J. M., Schneider, D. P., & Christensen, J. A. 1996, AJ, 111, 615
Press, W. H., & Schechter, P. 1974, ApJ, 187, 425
Raymond, J. C., & Smith, B. W. 1977, ApJS, 35, 419
Reichart, D. E., Castander, F. C., & Nichol, R. C. 1999a, ApJ, 516, 1
Reichart, D. E., Nichol, R. C., Castander, F. J., Burke, D. J., Romer, A. K., Holden, B. P., Collins, C. A., & Ulmer, M. P. 1999b, ApJ, 518, 521
Rocchia, R., Arnaud, M., Blondel, C., Cheron, C., Christy, J. C., Rothenflug, R., Schnopper, H. W., & Delvaille, J. P. 1984, A&A, 130, 53
Romer, A. K., Collins, C. A., Bohringer, H., Ebeling, H., Cruddace, R. C., & MacGillivray, H. T. 1994, Nature, 372, 75
Romer, A. K., et al. 2000, ApJS, 126, 209
Rosati, P., Della Ceca, R., Norman, C., & Giacconi, R. 1998, ApJ, 492, L21
Sadat, R., Blanchard, A., & Oukbir, J. 1998, A&A, 329, 21
Sarazin, C. L. 1998, X-Ray Emission from Clusters of Galaxies (Cambridge: Cambridge Univ. Press)
Schindler, S. 1999, A&A, 349, 435
Smail, I., Ivison, R. J., & Blain, A. W. 1997, ApJ, 490, L5
Snowden, S. L., et al. 1997, ApJ, 485, 125
Squires, G., Neumann, D. M., Kaiser, N., Arnaud, M., Babul, A., Böhringer, H., Fahlman, G., & Woods, D. 1997, ApJ, 482, 648
Sunyaev, R. A., & Zeldovich, Ya. B. 1972, Comments Astrophys. Space Phys., 4, 173
Tegmark, M. 1996, ApJ, 464, L35
Tormen, G. 1998, MNRAS, 297, 648
Tsuru, T. G., Matsumoto, H., Koyama, K., Tomida, H., Fukazawa, Y., Hattori, M., & Hughes, J. P. 1997, preprint (astro-ph/9711353)
van Haarlem, M. P., Frenk, C. S., & White, S. D. M. 1997, MNRAS, 287, 817
Viana, P. T. P., & Liddle, A. R. 1996, MNRAS, 281, 323
———. 1999, MNRAS, 303, 535
Vikhlinin, A., McNamara, B. R., Forman, W., Jones, C., Quintana, H., & Hornstrup, A. 1998a, ApJ, 502, 558
———. 1998b, ApJ, 498, L21
Vikhlinin, A., McNamara, B. R., Hornstrup, A., Quintana, H., Forman, W., Jones, C., & Way, M. 1999, ApJ, 520, L1
White, S. D. M., Efstathiou, G., & Frenk, C. S. 1993a, MNRAS, 262, 1023
White, S. D. M., Navarro, J. F., Evrard, A. E., & Frenk, C. S. 1993b, Nature, 366, 429
Wu, X. P., & Xue, Y. J. 2000, MNRAS, 311, 825